CO_2 dissolution in water using long serpentine microchannels

Thomas Cubaud,[a] Martin Sauzade, and Ruopeng Sun
Department of Mechanical Engineering, Stony Brook University, Stony Brook, New York 11794, USA

The evolution of carbon dioxide bubbles dissolving in water is experimentally examined using long microchannels. We study the coupling between bubble hydrodynamics and dissolution in confined geometries. The gas impregnation process in liquid produces significant flow rearrangements. Depending on the initial volumetric liquid fraction, three operating regimes are identified, namely saturating, coalescing, and dissolving. The morphological and dynamical transition from segmented to dilute bubbly flows is investigated. Tracking individual bubbles along the flow direction is used to calculate the temporal evolution of the liquid volumetric fraction and the average flow velocity near reference bubbles over long distances. This method allows us to empirically establish the functional relationship between bubble size and velocity. Finally, we examine the implication of this relationship during the coalescing flow regime, which limits the efficiency of the dissolution process. © *2012 American Institute of Physics*. [http://dx.doi.org/10.1063/1.3693591]

I. INTRODUCTION

The ability to control dissolving bubbles in liquids at the small scale is important for many applications including micro methanol fuel cells and carbon sequestration in porous media. Collapse and growth of bubbles under flow play an important role in blood circulation and during gas exchange in the respiratory system.[1] The system carbon dioxide-water is particularly important to the environment. When CO_2 dissolves in water, it forms a weak acid, which can affect the geochemistry of subsurface rocks as well marine organisms synthesizing shells.[2] A method for enriching minute amount of water with CO_2 on-chip would facilitate biological and chemical studies concerned with the impact of carbon dioxide on microenvironments.

Microfluidic devices provide useful platforms for examining the interactions between bubble dynamics and dissolution processes. Monodisperse bubbles can be produced one-by-one and their evolution can be readily tracked.[3–6] Segmented flows of bubbles are often used to enhance liquid/liquid mixing due to recirculation motion in the liquid plugs.[7–9] When bubbles are diffusive, this mechanism also facilitates gas absorption at the liquid interface. Indeed, the homogenization of the dissolved gas solute concentration in the bulk helps maintaining a sharp interfacial concentration gradient that enhances gas diffusion flux. The possibility to control different levels of CO_2 concentration in water on-chip offers new possibilities for integrated microsystems. Studies of time-dependent bubbles at the microscale, however, are relatively limited and the behavior of carbonated microflows has only been studied recently.[10,11] Hence, there is a need today for better understanding the morphology and hydrodynamic stability of dissolving bubbles at the microscale.

Here, we examine the behavior of diffusive bubble multiphase flows using long serpentine microchannels. A variety of regular trains of CO_2 bubbles are produced in water using a focusing section integrated on chip. Multiphase flows are monitored at the bubble level over very long distances with a high-speed camera and an inverted microscope. This method permits

---

a)Author to whom correspondence should be addressed. Electronic mail: thomas.cubaud@stonybrook.edu.

precise initial conditions in conjunction with a range of flow rates and pressures using hard microfluidic platforms. The large specific interfacial area of microscale bubbles favors diffusion. Dynamic rearrangements between bubbles, however, can significantly alter dissolution performance. To better understand the fundamentals of collapsing bubble microflows, the evolution of the bubble size and inter-spacing is measured for various flow rates and injection pressures. The morphological transition from segmented to dilute bubbly microflows is examined and we establish the bubble size-velocity relationship taking into account the local volumetric fraction. Over long distances, small bubbles convected in the parabolic flow profile can drift from their relative position in the train. For a specific range of initial sizes and liquid volumetric fractions, the dislocation in the relative bubble position in the arrangement can trigger cascade of coalescence events leading to the formation of a slow leading bubble. This mechanism significantly coarsens the flow and deteriorates the dissolution quality. We discuss the implications between collapsing bubble hydrodynamics and dissolution processes in constrained microgeometries.

II. EXPERIMENTAL SETUP

The microfluidic module is composed of silicon and glass materials. The observation channel consists of an etched-through double-side-polished silicon slice (height $h = 100$ μm), which is anodically bonded between two borosilicate glass plates. Such transparent, hard, and non-permeable microfluidic channels are particularly useful for examining liquid/gas multiphase flows in confined microgeometries.[12,13] Bubbles are generated at the junction between the fluids inlet channels. The junction is designed as a hydrodynamic focusing section and connected to a long serpentine microchannel [Fig. 1]. The observation channel is nearly square in cross-section with a width of $w \approx 87$ μm yielding an aspect ratio $h/w \approx 1.15$. To reduce the footprint of the device, the serpentine channel is composed of multiple channels arranged in parallel and connected with circular bends having a relatively large radius of curvature $R = 200$ μm for making a smooth flow transition between each channel. The total length of the serpentine microchannel is $L \sim 10$ cm, which allows for studying the evolution of multiphase flows over very long distance $L/w \sim 10^3$.

In the experiment, water is supplied to the chip using two high-pressure syringe pumps, each delivering a liquid volumetric flow rate of $Q_L/2$ in the side channels. The gas is injected from a pressurized tank. A flow meter is used to measure the inlet volumetric gas flow rate Q_G and a pressure sensor is embedded along the line to measure the gas injection pressure P_G. Here, experiments are conducted at near-room pressure for P_G ranging between 6 and 12 psig (i.e., between 1.4 and 1.8 atm) to sustain steady flows in long serpentine channels. A miniature regulator allows for precise gas pressure adjustments. The device is positioned on top of an inverted microscope with a high-intensity light emitting on the other side of the fluidic platform. For each set of pressure and injection flow rates, flow patterns are recorded using a high-speed camera.

III. BUBBLE FORMATION AND CRITICAL VOLUME FRACTION

Bubbles are produced at the junction made between the CO_2 gas inlet channel (central channel) and the water inlet channels (side channels) [Fig. 2(a)]. The distance x is measured
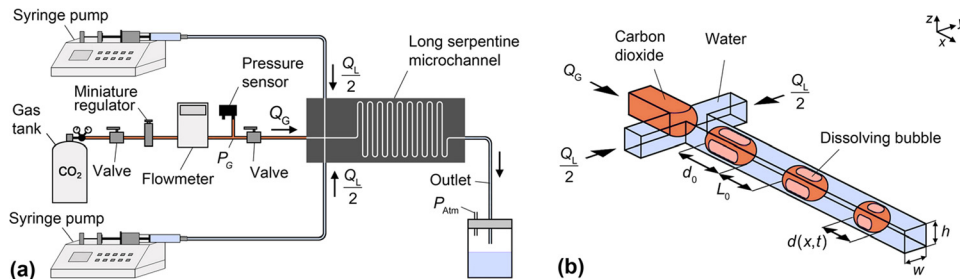

FIG. 1. (a) Schematics of experimental setup. (b) Generation of dissolving bubbles in hydrodynamic focusing section.
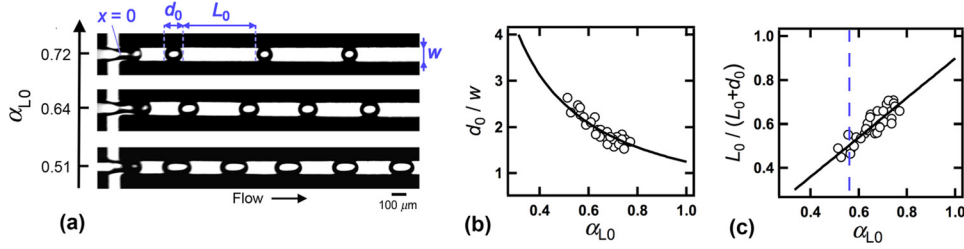
FIG. 2. Initial morphology of segmented flows. (a) Examples of CO$_2$ bubble generation at the focusing section for various initial volumetric liquid fractions α_{L0}. (b) Initial bubble size d_0 vs. volume fraction α_{L0} and solid line: $d_0/w = 1.25/\alpha_{L0}$. (c) Comparison between calculated liquid fraction $L_0/(L_0 + d_0)$ and injected volume fraction α_{L0} near the focusing section, solid line: $L_0/(L_0 + d_0) = k\,\alpha_{L0}$, with $k = 0.9$ and dashed-line: critical volume fraction $\alpha_{LC} = 0.55$.

along the main channel axis. The initial bubble size d_0 and spacing L_0 are recorded from experimental micrographs after bubble detachment from the inlet channel. The bubble size d_0 is measured between the tips of the two end-caps. Experiments are conducted from low to moderate Reynolds number Re varying between 1 and 50. For such moderate Re, bubbles detachment can occur in the main observation channel but this production method yields bubbles that are initially monodisperse in size and arrangement. Overall, the bubble size increases with the gas flow rate Q_G while the length of the liquid plugs increases with Q_L. Previous studies have shown that d_0 is inversely proportional to the initial volumetric liquid fraction $\alpha_{L0} = Q_L/(Q_L + Q_G)$ according to $d_0/w \approx a/\alpha_L$, with a being a prefactor depending the channel aspect ratio.[4,11] Here, we find that the value $a = 1.25$ yields a good fit of experimental data [Fig. 2(b)]. The normalized initial bubble length d_0/w is varied between 1.5 and 2.5 to probe bubble dynamics associated with the transition from segmented to bubbly flows and to evaluate the performance of the proposed CO$_2$ dissolution method in long serpentine microchannels.

In addition to determining the initial spatial distribution of the liquid and gas phases, the initial volumetric liquid fraction α_{L0} plays a critical role in the dissolution process. At standard ambient temperature and pressure (i.e., at 25 °C and 1 atm), the solubility of CO$_2$ in water is relatively low. When expressed in grams of solute per liter of solution, the solubility of CO$_2$ in water is $S \approx 1.5$ g/l.[14] Therefore, the minimal liquid fraction required to achieve complete CO$_2$ dissolution in water is $\alpha_{LC} = 1/(1 + S/\rho) \approx 0.55$, where the density of CO$_2$ is $\rho \approx 1.8$ g/l. This critical liquid volume fraction α_{LC} remains relatively independent of pressure P in our system since, on the one hand, the solubility S is proportional to pressure P according to Henry's law and reference data for pressure below one MPa,[15] and, on the other hand, the density ρ is also proportional to P assuming ideal gas behavior. Therefore, the parameter S/ρ should not depend on pressure and the critical volume fraction $\alpha_{LC} \approx 0.55$ is assumed independent of the gas injection pressure P_G.

In steady segmented flows, mass conservation between each bubble yields a simple relationship between the geometrical parameters d_0 and L_0 and the initial volume fraction according to $L_0/(L_0 + d_0) \sim Q_L/(Q_L + Q_G)$. Bubble measurement introduces an error due to the bubble caps and experimental data are fit with $L_0/(L_0 + d_0) \approx k\alpha_{L0}$, with the prefactor $k = 0.9$ [Fig. 2(b)]. This functional relationship is particularly useful for estimating the evolution of the volume fraction $\alpha_L(t)$ along the serpentine microchannel from micrographs. During dissolution, the effective gas flow rate along the channel decreases as $Q_G(t) = Q_G - Q_{Diff}(t)$, with Q_{Diff} being the rate of gas volume absorbed in the liquid, while the liquid flow rate Q_L remains essentially constant given the large difference between liquid and gas densities. Complete dissolution is obtained when the liquid fraction $\alpha_L = 1$, which should, in principle, be possible for multiphase flows formed when $\alpha_{L0} > \alpha_{LC}$.

IV. BUBBLE DISSOLUTION

A characteristic of diffusive multiphase flows is the transition from segmented flows to dilute bubbly flows. Convective liquid/gas mass transfer is enhanced in confined geometries

due to the recirculation motion inside the liquid plugs. This motion facilitates the homogenization of dissolved CO_2 in the water [Fig. 3(a)]. For a given set of flow parameters, the local bubble concentration varies in opposite way compared to the local CO_2 concentration in the liquid plugs. According to Fick's law,[16] mixing in the plugs is expected to increase the diffusion flux since the local reduction of CO_2 concentration in water near the bubble interface accentuates the concentration gradient ∇C. Here, we do not focus on the chemical reactions occurring between dissolved carbon dioxide and water but rather turn our attention to the dynamics of bubble collapse and its implication for multiphase flows in microgeometries.

The bubbles shrinkage is monitored along the flow direction from the temporal evolution of the characteristics of individual bubbles, such as position $x_B(t)$, size $d(t)$, and average distance to neighboring bubbles $L(t)$, with t being the time after breakup. Analyzing the temporal evolution of individual bubbles is more useful compared to the spatial evolution because of the variation of local average multiphase velocity $J_A = (Q_L + Q_G)/(hw)$ that depends on the rate of bubble collapse. Therefore, the method of description that follows individual bubbles (i.e., Lagrangian approach) is preferred to the method of description that focuses on the properties of the flow at a given location in space (i.e., Eulerian approach).

For elongated bubbles, the initial shrinkage rate depends on the gas inlet pressure P_G. The parameter $f = d_0/w - d(t)/w$ is useful for removal of the dependence on the initial size d_0 and is related to the diffusion volumetric flow rate according to $df/dt \sim Q_{diff}/hw$ for elongated bubbles $d > w$.[11] For relatively long periods of time ($t > 1$ ms), we previously showed that bubbles follow a Fickian behavior according to $f \sim t^{1/2}$. In the present study, we focus on detailed bubbles dynamics for relatively large pressure $P_G = 12$ psig and find that the function $f = at^{1/2}$, with $a = 4$ s$^{-1/2}$, approximates well experimental behavior for a range of initial bubble sizes d_0 [Fig. 3(b)]. Similar to our previous findings, data points collapse onto a master curve. For long time evolution, differences arise depending on the local CO_2 concentration and for small bubbles $d < w$, but overall the initial trend is similar.

The bubble size $d(x,t)$ plays an important role on diffusive multiphase flow dynamics. When $d > w$, the flow consists of arrays of elongated bubbles, or gas slugs, separated by continuous liquid plugs. This regime is usually referred to as segmented flow. For small sizes, when $d < w$, bubbles are not directly confined by the walls and adopt a spherical shape. This regime corresponds to the bubbly flow. A consequence of the bubble size reduction is the spatial transition from segmented flow (upstream region) to dilute bubbly flow (downstream region) [Fig. 3(c)]. The morphological evolution of bubbles as they progress along the channel induces complex dynamics. For instance, tiny bubbles appear to follow inclined trajectories in the parallel channels bending each bend. This mechanism, however, does not significantly influence the system and simple laws can be compared to experimental behavior.
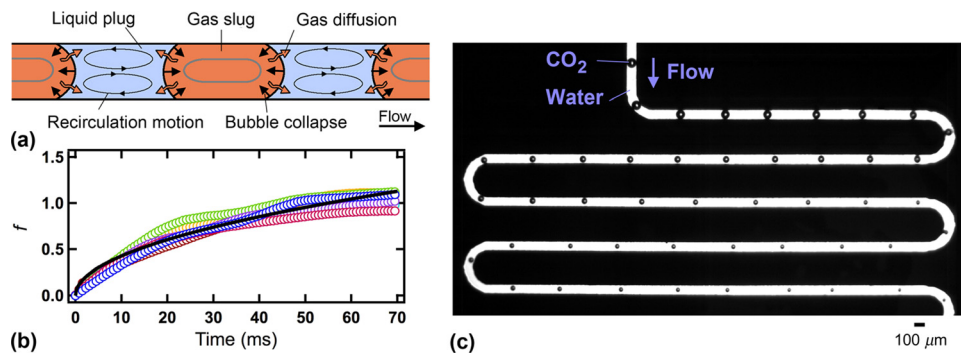

FIG. 3. Bubble dissolution process in long microchannel. (a) Schematic of enhanced gas/liquid diffusion mechanism. (b) Temporal evolution of $f = [d_0 - d(t)]/w$ for $P_G = 12$ psig with an initial volume fraction α_{L0} ranging between 0.56 to 0.77. Solid line: $f = at^{1/2}$, with $a = 4$ s$^{-1/2}$. (c) Transformation from segmented to dilute bubbly multiphase flows, $P_G = 10$ psig and $Q_L = 100$ μl min^{-1}.

The use of serpentine channels allows us to examine the long time evolution of flow morphologies. Lengthy channels also permit the building of rather large pressures, which is practical for enhancing gas dissolution processes. Given our long microchannel $L/w \sim 10^3$ and approximating a linear pressure drop, we label channel sections such as high-, medium-, and low-pressure regions. A complexity of this type of flow is rooted in the fact that the diminution of the local pressure $P(x)$ along the flow direction reduces solubility and slows down dissolution dynamics. Although the overpressure inside a bubble is inversely proportional to its radius r according to Young-Laplace law,[17] we experimentally find that dissolution rates do not necessarily self-accelerate for tiny bubbles and the bubble size appears to saturate in the downstream region. In the low-pressure region, we also observe instances where bubbles grow in size, possibly due to a combination of decompression and lower solubility effects. In addition, coalescence phenomena can significantly alter flow morphologies and dissolution efficiency. Over the range of parameters investigated, we identify three typical operating conditions depending on the initial volume fraction α_{L0}, namely "saturating regime" for $\alpha_{L0} < \alpha_{LC} \approx 0.55$, "coalescing regime" for α_{L0} ranging between 0.55 and 0.70, and finally "dissolving regime" for $\alpha_{L0} > 0.70$ [Fig. 4]. In the saturating regime, bubbles shrink in the high-pressure region but their size remains large ($d > w$) and relatively constant in the medium- and low-pressure regions. The flow is stable since bubbles are elongated and convected near the average multiphase flow velocity J_A. For larger α_{L0}, the transition from segmented to bubbly flow is accompanied with an increase of bubbles velocity V_B compared to J_A. Depending on the initial distance between bubbles L_0, neighboring bubbles may coalesce into larger bubbles. For large α_{L0}, however, coalescence events become rare and stable dilute bubbly flows of tiny bubbles are observed. The dissolving regime corresponds to an efficient operating regime for CO_2 dissolution in water using symmetric hydrodynamic focusing sections in microchannels. To better understanding this transition, in the following, we focus on the high-pressure region up to $x \sim 200w$.

V. TRANSITION FROM SEGMENTED TO BUBBLY FLOWS

During elongated bubble formation, the initial bubble size d_0 and distance L_0 are coupled through the initial volume fraction α_{L0}. In the course of the water impregnation process, the local bubble spacing L varies in a non-linear fashion with d. In particular, for segmented flows ($d > w$), the bubble spacing remains approximately constant $L \sim L_0$ [Fig. 5(a)]. By contrast, for bubbly flows ($d < w$), the spacing L is found to increase as bubbles collapse [Fig. 5(b)]. To quantify this phenomenon, we analyze experimental movies and track individual bubbles to measure the local spacing normalized by the initial spacing L/L_0 as a function of the scaled
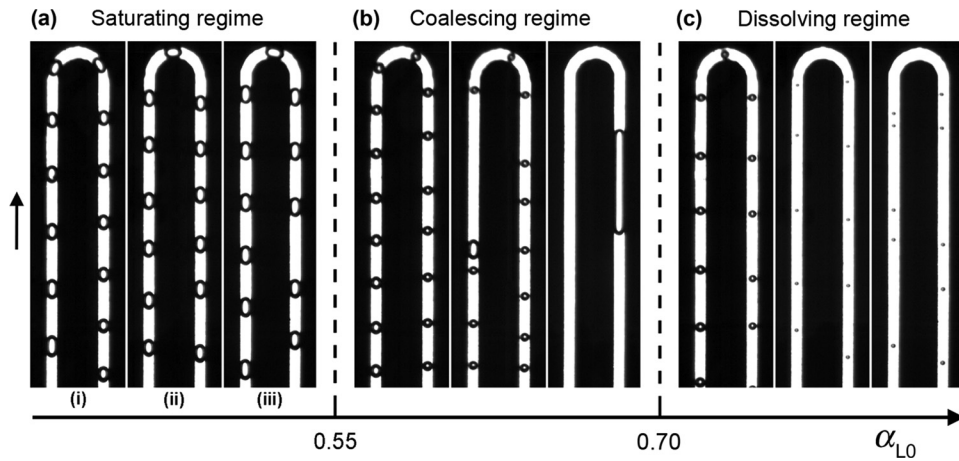

FIG. 4. Operating regimes as a function of initial volume fraction α_{L0}, spatial evolution of flow at various locations: (i) high-pressure region, $x/w \sim 50$, (ii) medium-pressure region, $x/w \sim 450$, and (iii) low-pressure region, $x/w \sim 900$. (a) Saturating regime, $\alpha_{L0} \approx 0.51$ and $P_G \approx 8$ psig. (b) Coalescing regime, $\alpha_{L0} \approx 0.63$ and $P_G \approx 10$ psig. (c) Dissolving regime, $\alpha_{L0} \approx 0.77$ and $P_G \approx 12$ psig.
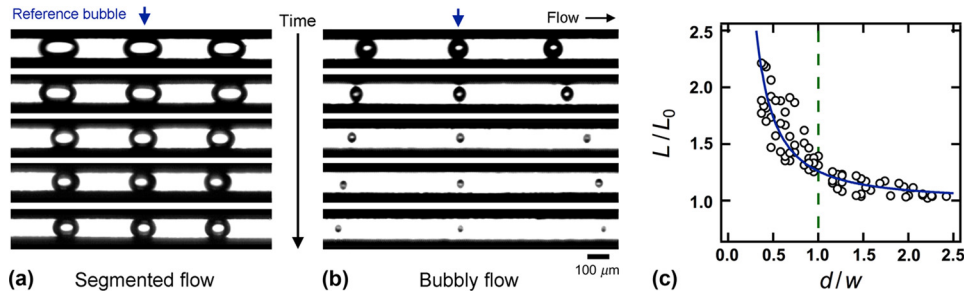
FIG. 5. Time-series of experimental micrographs showing structural evolution of dissolving CO_2 bubble flow pattern in the reference frame of the bubble. (a) Segmented flow ($d > w$), the bubble spacing L remains essentially constant. (b) Bubbly flow ($d < w$), the spacing L increases while the bubble size d decreases. (c) Evolution of normalized bubble spacing L/L_0 as a function of bubble size d/w for $P_G \approx 10$ and 12 psig and α_{L0} varying between 0.51 and 0.77, solid line: $L/L_0 = 1 + 0.26(d/w)^{-1.5}$.

bubble size d/w for various flow rates Q_L and Q_G and inlet pressure P_G [Fig. 5(c)]. In this graph, the distance between bubbles L is calculated as the average value between the spacing before and after the bubble of interest. Averaging is conducted because small bubbles may drift over time from their relative position. For bubbly flows, the distance in front is also relatively larger compared to the distance measured in the rear since the next bubble downstream is smaller and flows faster relative to the reference bubble. Overall, the evolution of the mean bubble spacing L can be predicted based on the instantaneous bubble size d and initial spacing L_0 according to $L/L_0 = 1 + 0.26(d/w)^{-1.5}$ [Fig. 5(c)]. The scatter in the data results in part from bubbles drifting and various initial flow conditions. The trend, however, corresponds to the characteristic morphological transition of dissolving multiphase microflows.

To elucidate the coupling between bubble size and velocity in relation with the evolution of the local volumetric fraction in dissolving flows, we focus on the data set corresponding to $P_G = 12$ psig with an initial volumetric volume fraction α_L ranging between 0.56 to 0.77. For various initial gas and liquid flow rates Q_G and Q_L, the position $x_B(t)$ and size $d(t)$ of a reference bubble is extracted from high-speed movies along with the mean spacing $L(t)$ between front and rear bubbles. The bubble position and spacing in the bends are interpolated from their values between two consecutive parallel channels. Data are then smoothed using a loess filter to dampen the effects of pixelization and obtain the average behavior. Optical measurements of the typical bubble size d and spacing L permit the computation of the effective liquid volume fraction α_L around the reference bubble according to

$$\alpha_L = \begin{cases} a \dfrac{L}{L+d} & \text{for } d > w \\ \dfrac{L + d - \pi d^3/(6hw)}{L+d} & \text{for } d < w \end{cases}, \tag{1}$$

where the coefficient a has been adjusted between 1.12 and 1.18 for each flow condition to match the volume fraction α_L calculated for bubbly flows when $d = w$. Given the initial scatter in the relationship between the injection volume fraction α_{L0} and the calculated initial fraction $L_0/(L_0 + d_0)$, the adjustment parameter a is in good agreement with the previously measured prefactor a $\approx 1/k$ used to fit data in Fig. 2(c). The temporal evolution of the calculated volume fractions α_L is shown in Figure 6(a). In particular, the liquid fraction is found to steadily increase for all flow rates with significantly faster rates for small and distant initial bubbles associated with flows having $\alpha_{L0} > 0.70$ as initial conditions.

The calculated velocities $V_B = dx_B/dt$ of reference bubbles for various flow rates are displayed in Figure 6(b). For segmented flows, the bubble speed typically decreases due the reduction in the multiphase flow superficial velocity J_A resulting from the volume gas loss by diffusion into the liquid. An opposite trend is observed for bubbly flows. In this case, the bubble velocity is found to increase over time before saturating for small bubbles.
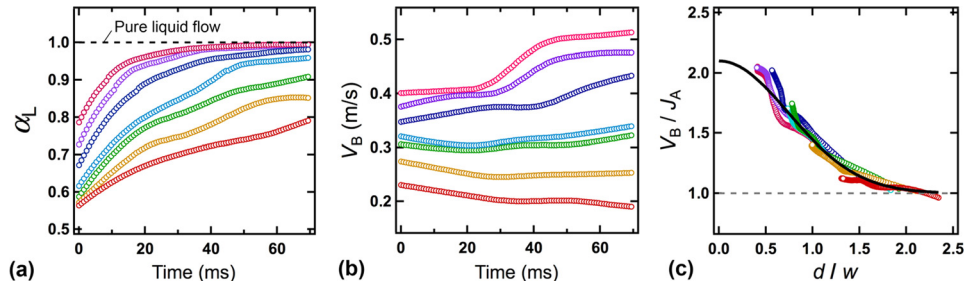
FIG. 6. (a) Evolution of volumetric liquid fraction α_L calculated using Eq. (1) for fixed inlet pressure $P_G = 12$ psig and different liquid injection flow rates, from top to bottom $Q_L = 130, 120, 110, 100, 90, 80$, and 70 μl min^{-1}. (b) Corresponding temporal evolution of bubble speeds V_B. (c) Bubble velocity normalized by local average flow velocity V_B/J_A as a function of scaled bubble size d/w, solid line: $V_B/J_A = 1 + 1.1\exp[-(d/w)^2]$ and dashed line: $V_B/J_A = 1$.

The relationship between bubble velocity and size in dissolving flows appears complex at first due to the evolution of the average velocity J_A. The information previously gained on the instantaneous liquid volume fraction α_L, however, permits to compute the average multiphase flow velocity according to $J_A = J_L/\alpha_L$, where $J_L = Q_L/(hw)$ is the superficial velocity of the liquid. Specific to liquid/gas flows, J_L is constant since the added volume of dissolved gas into the liquid is negligible given the density difference between the two phases. In Figure 6(c), we plot the bubble velocity V_B normalized by the average velocity J_A as a function of the instantaneous bubble size d/w. The calculated velocities align on a curve defined by a simple Gaussian function $V_B/J_A = 1 + 1.1\exp[-(d/w)^2]$. The boundary condition for $d = 0$ corresponds to the maximal velocity in a square channel $V_{max} = 2.1J_A$. The smooth transition for the bubble velocity indicates that V_B surpasses J_A for $d/w < 2$.

In this work, optical measurements of bubble size and spacing permit to decorrelate bubble hydrodynamics from dissolution processes. This study of small bubbles dynamics complements theories of elongated bubble motion in confined geometries[18–21] when the normalized bubble velocity scales as Ca$^{2/3}$, where the capillary number Ca compares the ratio of viscous to surface tension forces. Here, our experimental findings indicate that a scaling solely based on Ca is inadequate for describing collapsing bubble micro-dynamics when $d < 2w$, since the capillary number remains nearly constant in our case (assuming only small changes in bubble velocity, surface tension, and viscosity during dissolution). The non-linearity between bubble speed and size, however, is prone for flow instabilities during the water enrichment process.

VI. COALESCENCE

The structural stability of multiphase flows is important for the efficiency of the CO_2/water mixing process. The relative change in bubble velocity as bubbles shrink can induce recombination processes. This mechanism is overall detrimental to dissolution since the liquid/gas interfacial area is reduced. Although the initial bubble size is relatively uniform for a set of flow parameters, small fluctuations are observed in size and spacing between neighboring bubbles. These perturbations are amplified during the transition from segmented to bubbly flows due to velocity differential between bubbles of different sizes. A single coalescence event between neighboring bubbles can cause the system bifurcation and triggers a chain-reaction of subsequent coalescence events.

A case study of multiple coalescence events is displayed in Figure 7 with a time-series of a coalescing reference bubble along with its corresponding velocity and size as a function of time. We denote the number of successive coalescence events by C, where $C = 0$ corresponds to no coalescence, $C = 1$ corresponds to one coalescence, and so on. The reference bubble was produced at a slightly larger size compared to its neighbor due to random fluctuations. The size difference induces a dislocation in the flow pattern arrangement. The dislocation is further amplified as bubbles shrink and the reference bubble eventually coalesce with its upstream
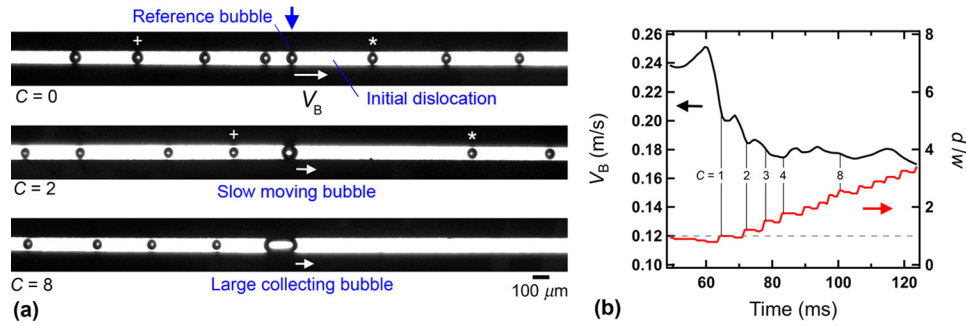
FIG. 7. (a) Time-series of the evolution of a large reference bubble leading to the deterioration of diffusive multiphase flows, the symbols + and * are used to label specific bubbles (reference frame: bubble front). (b) Correlation between bubble velocity and bubble size during a coalescence cascade, C is the number of coalescence events; dashed line: $d/w = 1$.

neighbor. The outcome of the first coalescence produces a large bubble ($d > w$) with a significantly lower speed [Fig. 7(b)—$C = 1$]. This slow moving bubble is rapidly caught up by smaller bubbles on its trail and grows into a large collecting bubble. Although the growth of the leading bubble occurs by step with each coalescence event, the bubble growth rate appears nearly linear with time and bubble velocity is practically constant when $d > 2w$, which is in accordance with our results on bubble velocity. This type of scenario, where the system bifurcates toward a self-degrading dissolution quality due to the effect of surface tension forces, is typical of the coalescing regime [Fig. 4(b)].

VII. CONCLUSION

In this study, we discuss the properties and operating conditions of a simple CO_2/water continuous micromixer. Dissolving microbubbles are produced using a hydrodynamic focusing section connected to a long serpentine channel. For the carbon dioxide-water fluid pair, the saturation concentration of dissolved gas in liquid corresponds to a volumetric liquid volume fraction $\alpha_{LC} \approx 0.55$, which is independent of injection pressure near atmospheric conditions. The relationship between the phase distribution (i.e., bubble size and spacing) and the initial volumetric liquid fraction α_{L0} in microchannels is established. Three characteristic regimes, including saturating, coalescing, and dissolving are located as a function of α_{L0}. We examine the morphological and dynamical transition from segmented to dilute bubbly flows. For segmented flows, the bubble spacing remains approximately constant, while for bubbly flows, the bubble spacing increases when bubbles shrink. Monitoring individual bubbles along the flow direction is used to calculate the temporal evolution of the liquid volumetric fraction, which in turn is utilized for computing the average flow velocity at the reference bubble location. Experimental findings show that the instantaneous bubble velocity normalized by the average flow velocity is a simple function of the bubble size. Finally, we examine the implication of this relationship during coalescing flows that severely limit the efficiency of the dissolution process.

For practical applications, the dissolving regime appears optimum for achieving CO_2 dissolution in water using a simple microfluidic apparatus. Various target CO_2 concentrations in water can be realized for $\alpha_{L0} > 0.70$. Microfluidic systems connected to pressurized inlet and outlet ports would permit a wider range of CO_2 mass concentration in water. In particular, since fast dissolution dynamics are expected at large pressures, devices operating at large pressures may prevent drifting bubbles from merging before attaining the plateau velocity (i.e., near the maximal velocity of the parabolic profile), which should, a priori, suppress the coalescing regime. The saturating flow regime is also of interest due to its robust hydrodynamic stability and the possibility for reaching the saturation limit of CO_2 concentration in water. In this case, segmented flow with long bubbles is advantageous because bubbles can make direct contact with the walls depending on dynamic wetting conditions and be removed from the flow using hydrophobic porous membranes.[22,23] A variety of microfluidic designs can be implemented to circumvent current limitations in the manipulation of carbonated microflows.

[1] J. B. Grotberg, Phys. Fluids **23**, 021301 (2011).
[2] S. C. Talmage and C. J. Gobler, Proc. Natl. Acad. Sci. U. S. A. **107**, 17246 (2010).
[3] P. Garstecki, H. A. Stone, and G. W. Whitesides, Phys. Rev. Lett. **94**, 164501 (2005).
[4] T. Cubaud, M. Tatineni, X. Zhong, and C.-M. Ho, Phys. Rev. E **72**, 037302 (2005).
[5] N. Dietrich, S. Poncin, N. Midoux, and H. Z. Li, Langmuir **24**, 13904 (2008).
[6] W. van Hoeve, B. Dollet, M. Versluis, and D. Lohse, Phys. Fluids **23**, 092001 (2011).
[7] A. Günther, M. Jhunjhunwala, M. Thalmann, M. A. Schmidt, and K. F. Jensen, Langmuir **21**, 1547 (2005).
[8] J. Aubin, M. Ferrando, and V. Jiricny, Chem. Eng. Sci. **65**, 2065 (2010).
[9] C. Y. Lee, C. L. Chang, Y. N. Wang, and L. M. Fu, Int. J. Mol. Sci. **12**, 3263 (2011).
[10] J. I. Park, Z. Nie, A. Kumachev, and E. Kumacheva, Soft Matter **6**, 630 (2010).
[11] R. Sun and T. Cubaud, Lab Chip **11**, 2924 (2011).
[12] T. Cubaud and C.-M. Ho, Phys. Fluids **16**, 4575 (2004).
[13] T. Cubaud, U. Ulmanella, and C.-M. Ho, Fluid Dyn. Res. **38**, 772 (2006).
[14] D. R. Lide, *CRC Handbook of Chemistry and Physics* (Taylor & Francis, Boca Raton, FL, 2007).
[15] J. Carroll, J. D. Slupsky, and A. E. Mather, J. Phys. Chem. Ref. Data **20**, 1201 (1991).
[16] R. B. Bird, W. E. Stewart, and E. N. Lightfoot, *Transport Phenomena* (Wiley, New York, 2007).
[17] P. G. de Gennes, F. Brochard-Wyart, and D. Quéré, *Capillarity and Wetting Phenomena* (Springer Science+Business Media, LLC, New York, 2004).
[18] F. P. Bretherton, J. Fluid Mech. **10**, 166 (1961).
[19] J. Ratulowski and H.-C. Chang Phys. Fluids A **1**, 1642 (1989).
[20] H. Wong, C. J. Radke, and S. Morris, J. Fluid Mech. **292**, 71 (1995).
[21] M. T. Kreutzer, F. Kapteijn, J. A. Moulijn, and J. J. Heiszwolf, Chem. Eng. Sci. **60**, 5895 (2005).
[22] D. D. Meng, T. Cubaud, C.-M. Ho, and C.-J. Kim, J. Microelectromech. Syst. **16**, 1403 (2007).
[23] C. C. Liu, J. A. Thompson, and H. H. Bau, Lab Chip **11**, 1688 (2011).